Chapter 16
Experimental Fluid-Structure Interaction of Airflow Over a Cylinder with an Attached Cantilever Plate in a Wind Tunnel

D. T. Will and W. D. Zhu

Abstract The aim of this fluid-structure interaction work is to explore the vibration response of a stiff cantilever plate attached to a cylinder in an AEROLAB Educational Wind Tunnel under an airflow excitation. An accelerometer-based experimental modal analysis is first used to determine the first three out-of-plane natural frequencies and mode shapes of the experimental structure within a frequency band of 0-400 Hz. Using constant temperature anemometry with a wind tunnel free-stream velocity of 10 m/s and a Reynolds number on the order of 2.1×10^4, a single-channel hot-wire anemometer probe is roved throughout the flow-field. The velocity variations in the airflow over the cylinder and cantilever plate are measured and the data is processed to observe the mean airflow velocity around the structure. Then, the structure's response to a free-stream velocity of 10 m/s, yielding a maximum measured Strouhal vortex shedding frequency of approximately 40.3 Hz, is measured using an accelerometer-based operational modal analysis to capture the first two natural frequencies and mode shapes within a frequency band of 0-400 Hz.

Keywords Fluid-structure interaction · Modal analysis

INTRODUCTION

Fluid-structure interaction (FSI) can be defined as the dynamics of a structure's response to an input caused by a working fluid, such as air or water, coupled by the subsequent effects the structure has on that working fluid [1]. In the literature, various test and numerical simulation configurations have been studied, including attached [2] or detached [3] splitter plates, rigid or flexible splitter plates [4], and splitter plates placed either in front of [5] or behind [6] a circular cylinder. Other cases studied include flow past a square prism [7], a cantilever plate with no cylinder [8], flexible wings in transverse gusts [9], and shock-wave/boundary-layer interaction in supersonic flow [10]. Typical fluid mediums tested or simulated include air, water, and other incompressible fluids such as glycerin [11]. For air, the range of Reynolds numbers examined was from 3.83×10^4 to 3.9×10^7 m^{-1}, while for water and other incompressible fluids, the range of Reynolds numbers examined was from 100 to 9.5×10^5. Most FSI research in the literature focuses on large, nonlinear deformation of a structure, while the current work examines small vortex-induced vibrations that are not visible to the naked eye. This work seeks to expand upon the current research by studying the vibration of a rigid cantilever plate attached to a rigid cylinder using the measurement techniques of experimental modal analysis (EMA) with roving impact hammer excitation and operational modal analysis (OMA) with airflow excitation and a roving accelerometer. Further, the flow field around the cylinder and cantilever plate will be examined using constant temperature anemometry (CTA), or hot-wire anemometry, to understand the mechanism by which vortex shedding excites the test specimen.

Background

The design for the experimental setup was developed given size constraints for the experiment in an AEROLAB Educational Wind Tunnel (EWT) where the test section is 304.8 mm wide, 304.8 mm tall, and 609.6 mm long [12]. The cylinder diameter selection was determined by a tradeoff between manufacturability and vortex shedding frequency. The frequency, f, of vortex

D. T. Will · W. D. Zhu
Department of Mechanical Engineering, University of Maryland, Baltimore County, 1000 Hilltop Circle, Baltimore, MD 21250
e-mail: dwill1@umbc.edu; wzhu@umbc.edu

Brandon Dilworth et al. (eds.), *Topics in Modal Analysis & Parameter Identification I, Vol. 9*, Conference Proceedings of the Society for Experimental Mechanics Series, https://doi.org/10.13052/97887-438-0154-2_16

shedding over a cylinder is calculated using the Strouhal number, *St*, [1]

$$f = \frac{St \times V}{D} \tag{1}$$

where *V* is the airflow velocity, *D* is the diameter of the cylinder, and the Strouhal number is given by Massey and Ward-Smith [13]

$$St = 0.198\left(1 - \frac{19.7}{Re}\right), 250 < Re < 2 \times 10^5 \tag{2}$$

or by Modarres-Sadeghi [1] as $St = 0.2,\ 300 < Re < 300{,}000$. The Reynolds number, *Re*, is defined by [14]

$$Re = \frac{\rho V D}{\mu} \tag{3}$$

where $\rho = 1.204\ \frac{kg}{m^3}$ and $\mu = 1.825 \times 10^{-5}\ \frac{kg}{m \cdot s}$ for air at normal temperature and pressure, i.e., air at 20°C and 101,325 Pa. The Reynolds number of air over a cylinder plotted as a function of the air velocity for various cylinder diameters is shown in Fig. 1 and the vortex shedding frequency of air over a cylinder plotted as a function of the air velocity for various cylinder diameters is shown in Fig. 2. A cylinder diameter of 31.8 mm was chosen, which yields a vortex shedding frequency of 28 Hz to 402 Hz over the wind tunnel velocity range of 4.5 m/s to 64.5 m/s.

EMA Setup and Results

An experimental structure was designed, machined, and assembled as described in Will and Zhu [12]. A modification to the upper mounting bracket was made to accommodate the use of a newer manufactured AEROLAB EWT where the upper mounting configuration was different from the older manufactured AEROLAB EWT used in Will and Zhu [12]. The new upper mounting bracket was 517.5 mm in length and the location of the mounting hole used to fasten the cylinder was shifted to accommodate the newer manufactured AEROLAB EWT. The experimental setup mounted inside the newer manufactured AEROLAB EWT is shown in Fig. 3.

Due to the different boundary conditions from the modified upper mounting bracket between the older manufactured EWT in Will and Zhu [12] and the newer manufactured EWT, an EMA was performed to determine the experimental setup's first three out-of-plane natural frequencies and mode shapes. One PCB Piezotronics, Inc. 352C66 single-axis accelerometer was placed on the far-side of the cylinder, cantilever plate, and upper and lower mounting brackets, where the far side is defined as the side of each component facing into the page in Fig. 3(a) and the near side is defined as the side of each component facing out of the page in Fig. 3(a). Additionally, a PCB Piezotronics, Inc. 086C01 modally tuned impact hammer with a nylon tip, four PCB Piezotronics, Inc. 080A15 adhesive mounting bases, PCB Piezotronics, Inc. 080A109 adhesive

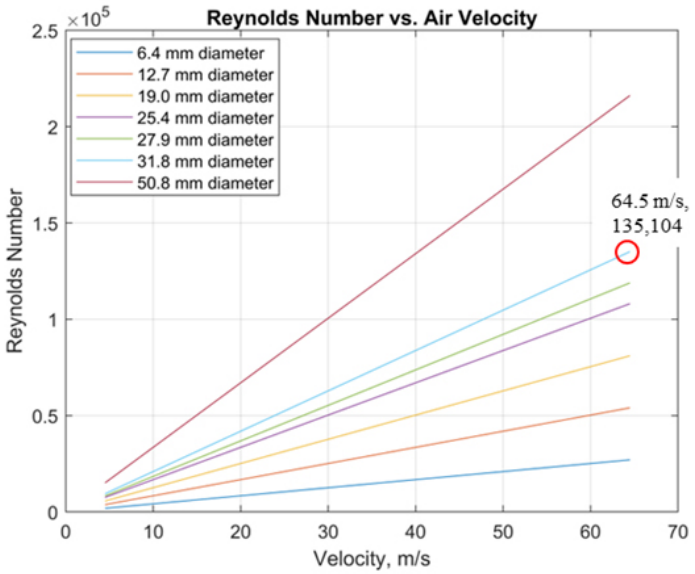

Fig. 1 A plot of the Reynolds number versus the airflow velocity for various cylinder diameters. The red circle indicates the maximum Reynolds number at the highest airflow velocity for the selected cylinder diameter of 31.8 mm.

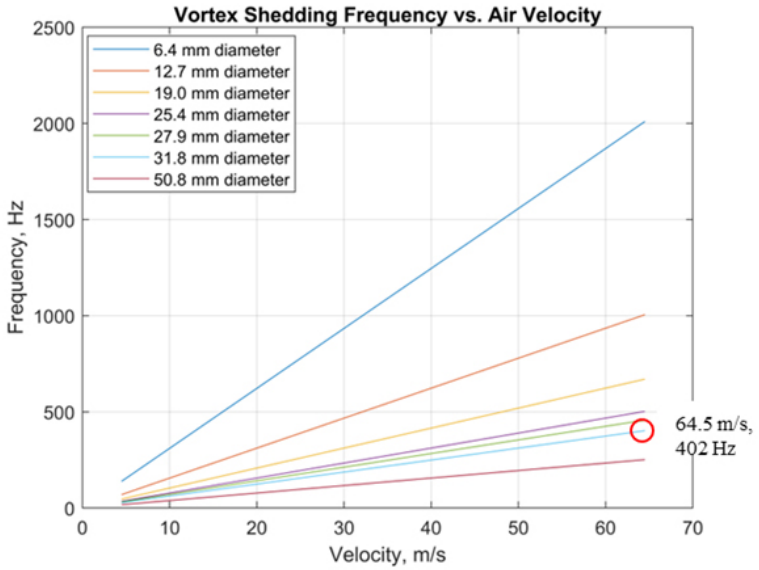

Fig. 2 A plot of the vortex shedding frequency versus the airflow velocity for various cylinder diameters. The red circle indicates the maximum vortex shedding frequency at the highest airflow velocity for the selected cylinder diameter of 31.8 mm.

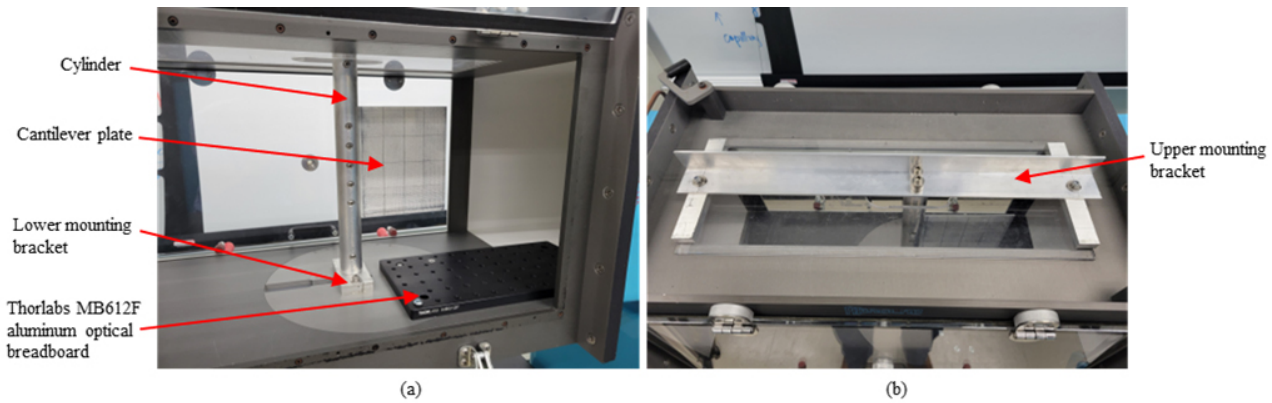

Fig. 3 Experimental setup inside the AEROLAB EWT including the (a) cylinder, cantilever plate, lower mounting bracket, Thorlabs MB612F aluminum optical breadboard, and (b) the upper mounting bracket.

wax, a Siemens Signal Conditioning and Data Acquisition System (SCADAS) Mobile SCM2E02V, and Siemens Testlab Version 2306 software were used to perform the EMA. The setup and equipment used for the EMA is shown in Fig. 4. A roving hammer test was performed using 37 impact locations, or nodes, where 4 nodes were used on the cylinder, 25 nodes were used on the cantilever plate, 5 nodes were used on the upper mounting bracket, and 3 nodes were used on the lower mounting bracket. Each node was impacted three times to compute an average of three frequency response functions (FRFs) for a total of 111 hammer impacts on the structure. The model of the experimental structure generated using Testlab is shown in Fig. 5, where the gray boxes indicate the node or impact locations, and the red circles indicate the locations of the reference accelerometers placed on the far side of the experimental structure.

After the roving hammer testing was completed, Testlab's PolyMAX algorithm was used to curve fit the FRFs using a curve fitting model size of 25 modes. The first three stable modes and their corresponding mode shapes were selected within a frequency band of 0-400 Hz, as shown in Figs. 6 and 7, respectively. As indicated in Fig. 7, mode 1 is the first bending mode of the cantilever plate, mode 2 is the first torsional mode of the cantilever plate, and mode 3 is an out-of-plane bending mode of the cylinder with minor out-of-plane bending of the cantilever plate. The modal assurance criterion (MAC) values are presented in Table 1, where values close to 0 indicate low correlation between mode shapes and values close to 1 indicate

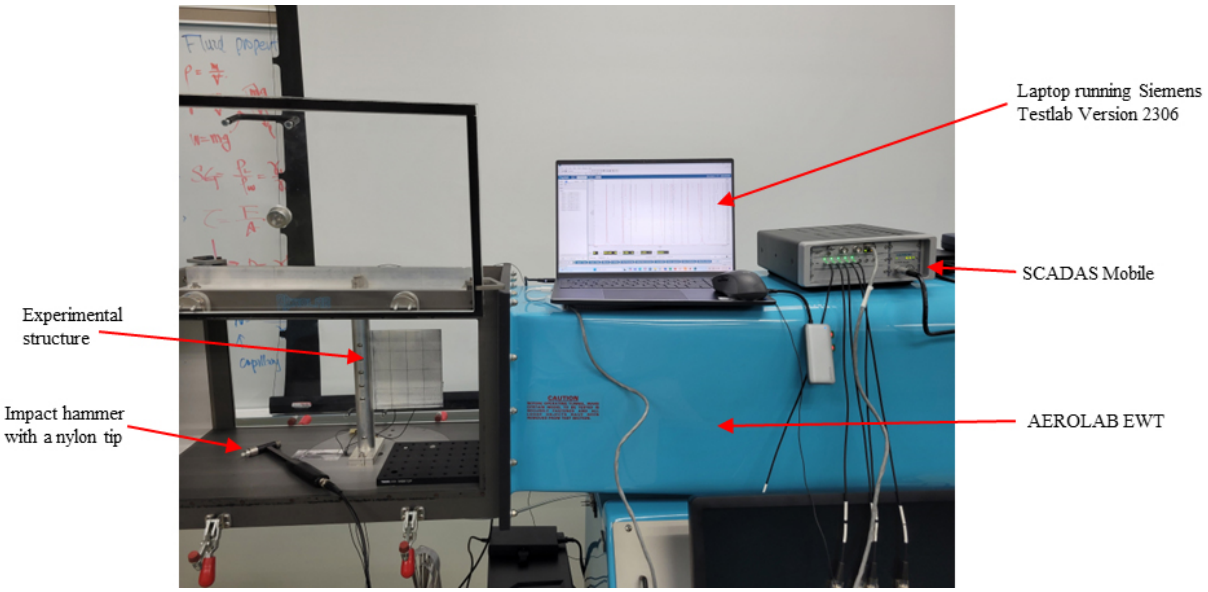

Fig. 4 Setup and test equipment used for the EMA including the AEROLAB EWT, experimental structure, impact hammer with a nylon tip, laptop running Siemens Testlab Version 2306, and SCADAS Mobile.

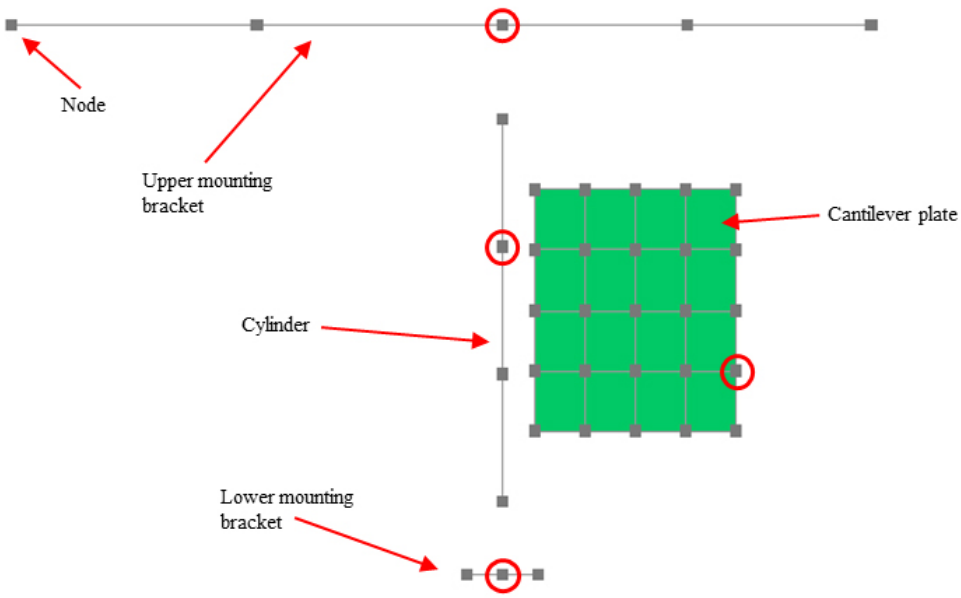

Fig. 5 Model of the experimental structure developed in Siemens Testlab Version 2306 software, where the nodes are indicated by the gray boxes and the red circles indicate the locations of the reference accelerometers placed on the far side of the experimental structure.

high correlation between mode shapes. The mode shapes in Fig. 7 and the MAC values in Table 1 indicate that modes 1 and 2 are unique, with a MAC value of 0.001, modes 1 and 3 share some similarities in cantilever plate bending, yielding a MAC value of 0.241, and modes 2 and 3 are unique, with a MAC value of 0.055.

CTA Setup and Results

A CTA experiment was performed using a Dantec Dynamics MiniCTA 54T42, 55P16 hot-wire probe, hot-wire calibrator, laptop running StreamWare Basic V7.00 software, and a National Instruments NI-9215 data acquisition board for capturing the measurements from the MiniCTA 54T42 at 10 kHz. Additionally, a hot-wire probe holder was designed and a machined,

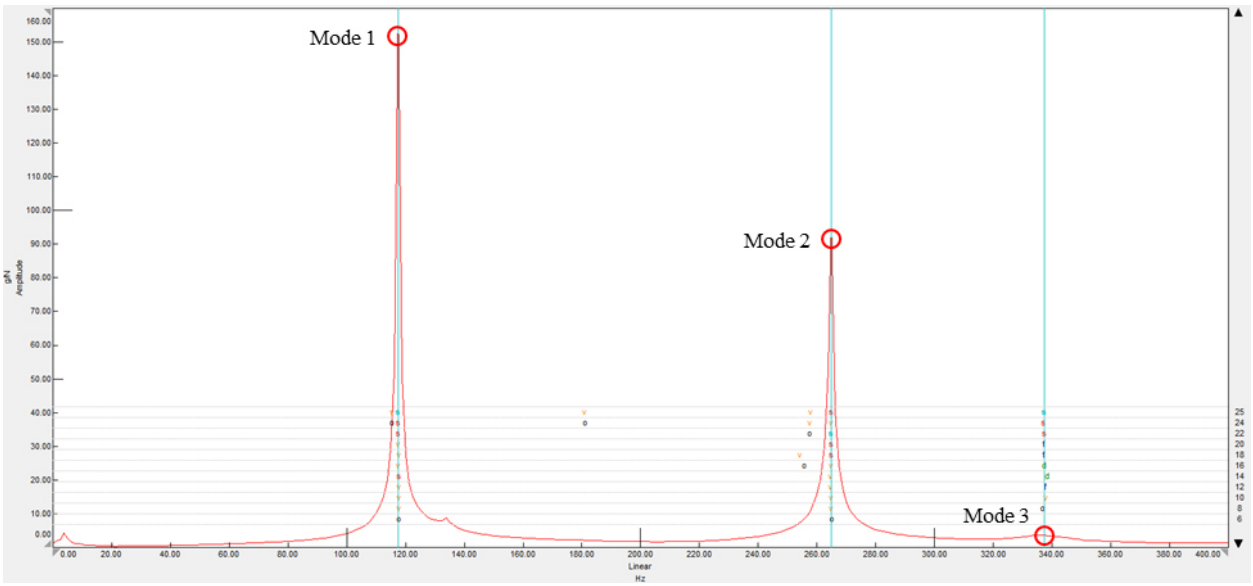

Fig. 6 Stabilization diagram using a curve fitting model size of 25 modes, where the first three stable modes between a frequency band of 0-400 Hz are indicated by red circles.

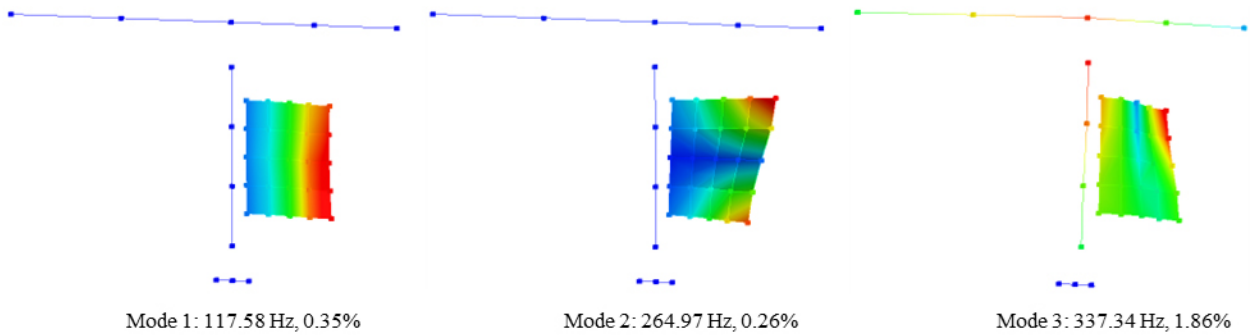

Fig. 7 First three stable mode shapes and their corresponding frequency and damping values within a frequency band of 0-400 Hz.

Table 1 MAC values for the EMA mode shapes.

EMA / EMA	**Mode 1** (117.58 Hz)	**Mode 2** (264.97 Hz)	**Mode 3** (337.34 Hz)
Mode 1 (117.58 Hz)	1.000	0.001	0.241
Mode 2 (264.97 Hz)	0.001	1.000	0.055
Mode 3 (337.34 Hz)	0.241	0.055	1.000

which was mounted to a Thorlabs XYR1 translation and rotation stage for correct positioning of the probe during the experiment. Prior to performing the CTA experiment, a calibration of the hot-wire probe was performed. The 55P16 probe was installed onto the hot-wire calibrator and a steady flow of filtered air was supplied through the calibrator. A calibrated Traceable 38RJ43 digital barometer was used to measure the ambient pressure and a Klein Tools multimeter was used to measure the hot-wire calibrator's thermistor resistance for entry into the calibration software. After completion of the calibration procedure, the StreamWare Basic v7.00 software generated a calibration curve for accurately converting the measured voltages to airflow velocities. The complete CTA setup and equipment used for measuring the airflow velocities and the CTA calibration setup and equipment is shown in Figs. 8 and 9, respectively.

After calibration, the translation and rotation stage, hot-wire probe holder, and hot-wire probe were installed into the AEROLAB EWT, as shown in Figs. 10 and 11. Using the optical breadboard and the translation and rotation stage, the hot-

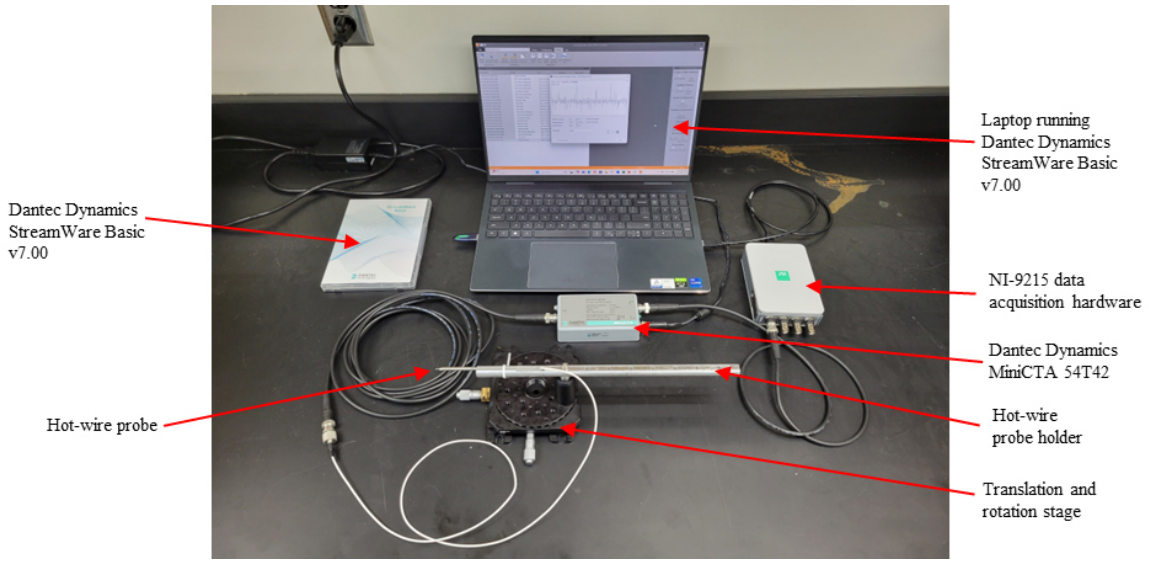

Fig. 8 CTA setup and equipment used to measure the airflow velocities around the cylinder and cantilever plate including the Dantec Dynamics MiniCTA 54T42, hot-wire probe, hot-wire probe holder, NI-9215 data acquisition hardware, laptop running Dantec Dynamics StreamWare Basic v7.00, and translation and rotation stage.

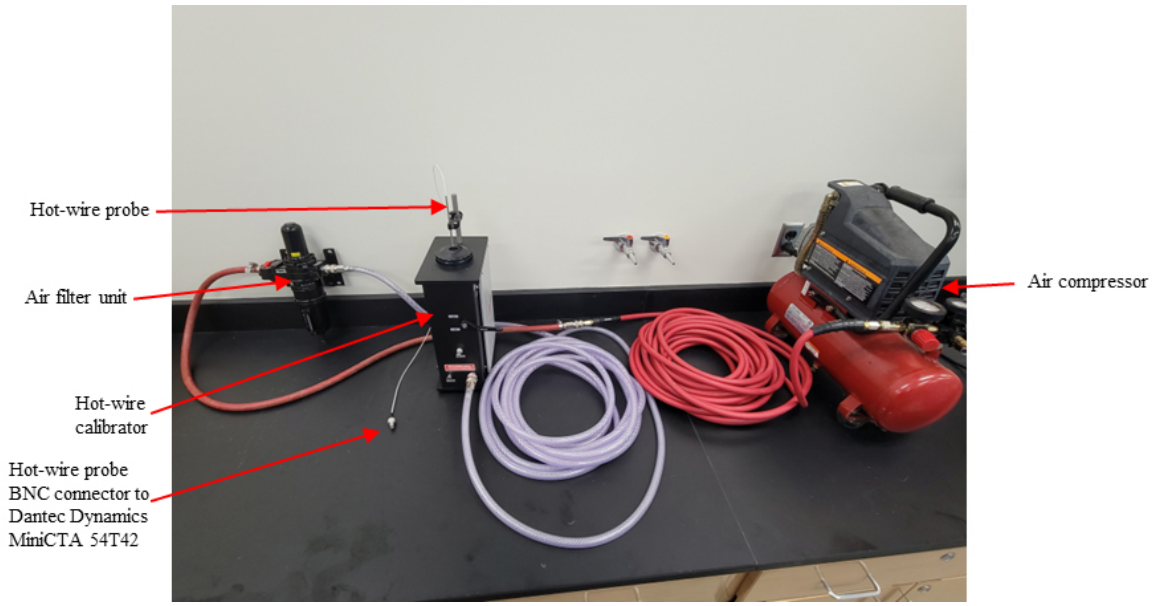

Fig. 9 CTA calibration setup and equipment including the hot-wire probe, hot-wire calibrator, air filter unit, and air compressor.

wire probe was roved through 120 points around the cylinder and cantilever plate. Referencing the origin of the coordinate axes in Fig. 11, the hot-wire probe was roved through each combination of the following positions:

- X: 0 mm, 25.39 mm, 50.79 mm, 76.19 mm, 101.60 mm, 127.00 mm, 152.40 mm, 177.80 mm
- Y: -6.34 mm, -31.75 mm, -57.15 mm, -82.55 mm, -107.90 mm
- Z: 12.69 mm, 25.39 mm, 38.09 mm

The wind tunnel free-stream velocity was set to 10 m/s and 10 s of data were collected at each of the 120 points.

After the CTA experiment was completed, the voltage data were converted into airflow velocities using the calibration curve and the mean airflow velocities at each of the 16 measurement planes were plotted. Planes along the X-axis, Y-axis, and Z-axis are shown in Figs. 12, 13, and 14, respectively.

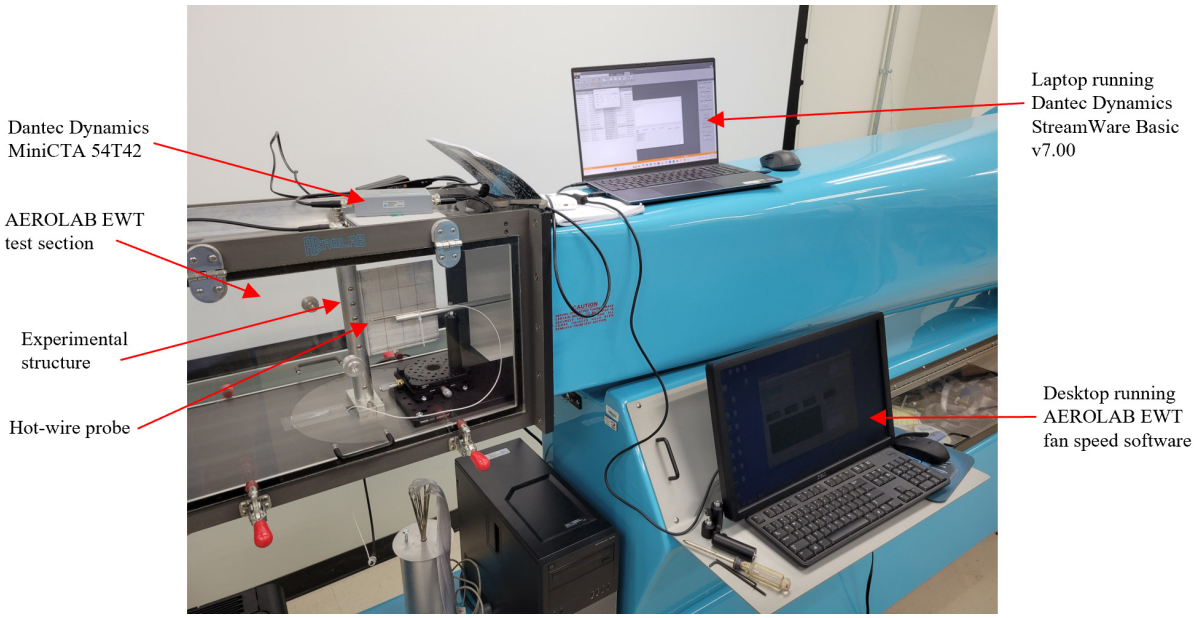

Fig. 10 Setup and test equipment used for the CTA experiment including the AEROLAB EWT with desktop computer and software for controlling the fan speed, experimental structure, hot-wire probe, Dantec Dynamics MiniCTA 54T42, and laptop running Dantec Dynamics StreamWare Basic v7.00.

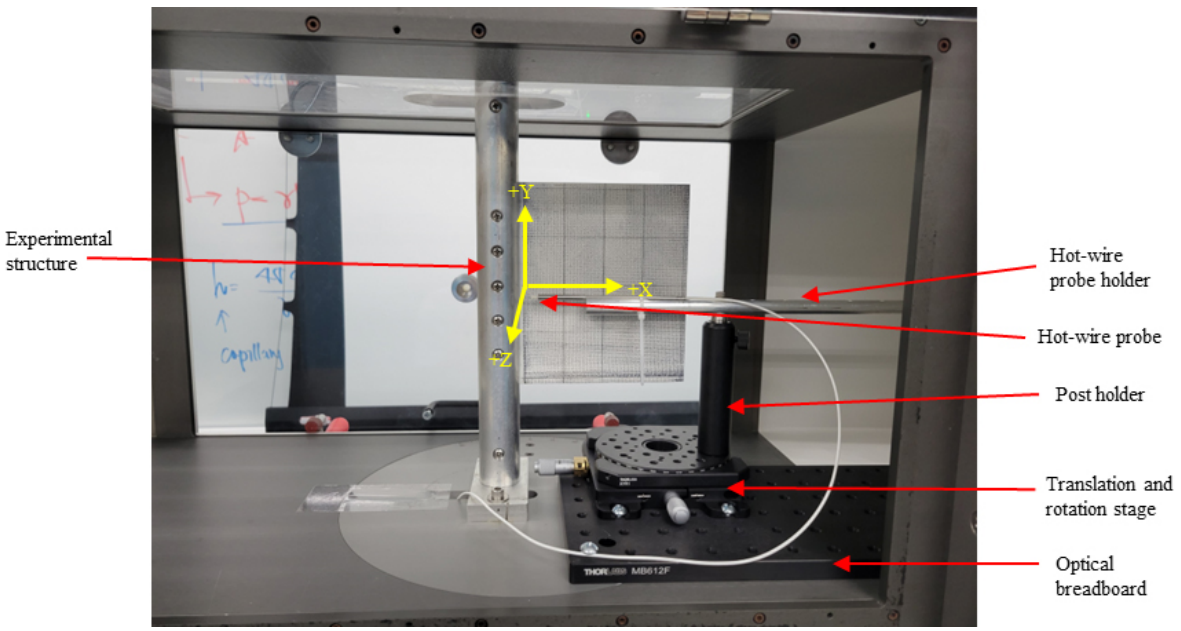

Fig. 11 Setup and test equipment used for the CTA inside the EWT test section including the experimental structure, hot-wire probe, hot-wire probe holder, post holder, translation and rotation stage, and optical breadboard. The coordinate axes defining the CTA coordinate directions used in the experiment are also depicted.

OMA Setup and Results

An OMA experiment was performed in the AEROLAB EWT using the CTA equipment as well as the SCADAS Mobile, a single roving accelerometer, four fixed reference accelerometers, and a laptop running both Siemens Testlab Version 2306 and Dantec Dynamics StreamWare Basic v7.00. Prior to conducting the experiment, a calibration of the hot-wire probe was performed and a calibration curve was obtained. During the experiment, the wind tunnel was set to a free-stream velocity of 10 m/s and the hot-wire probe was kept in a constant position at X = 127.00 mm, Y = -31.75 mm, and Z = 25.39 mm, while

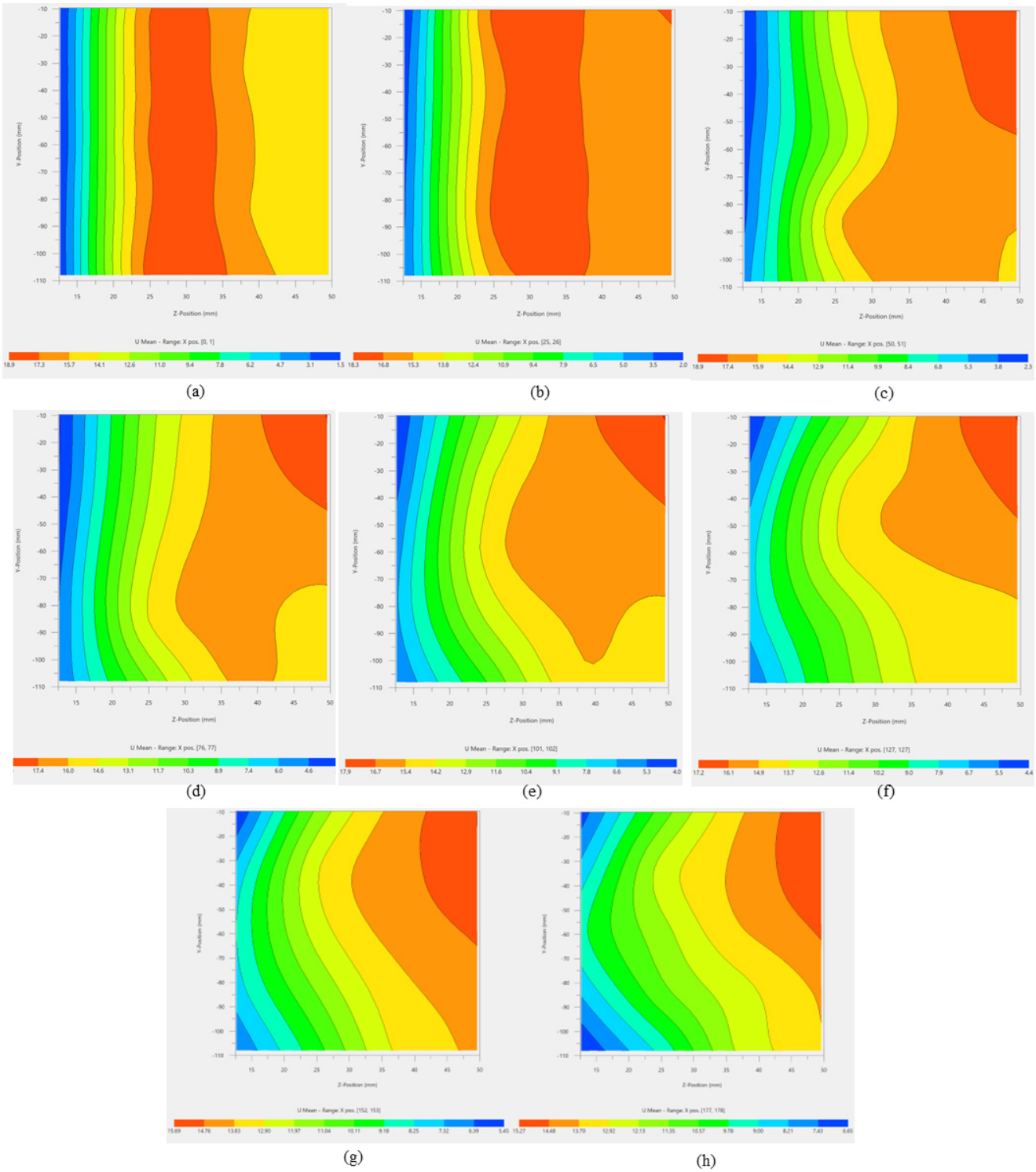

Fig. 12 Mean airflow velocity around the cylinder and cantilever plate at planes (a) X = 0 mm, (b) X = 25.39 mm, (c) X = 50.79 mm, (d) X = 76.19 mm, (e) X = 101.60 mm, (f) X = 127.00 mm, (g) X = 152.40 mm, and (h) X = 177.80 mm captured using CTA measurements at a wind tunnel free-stream velocity of 10 m/s.

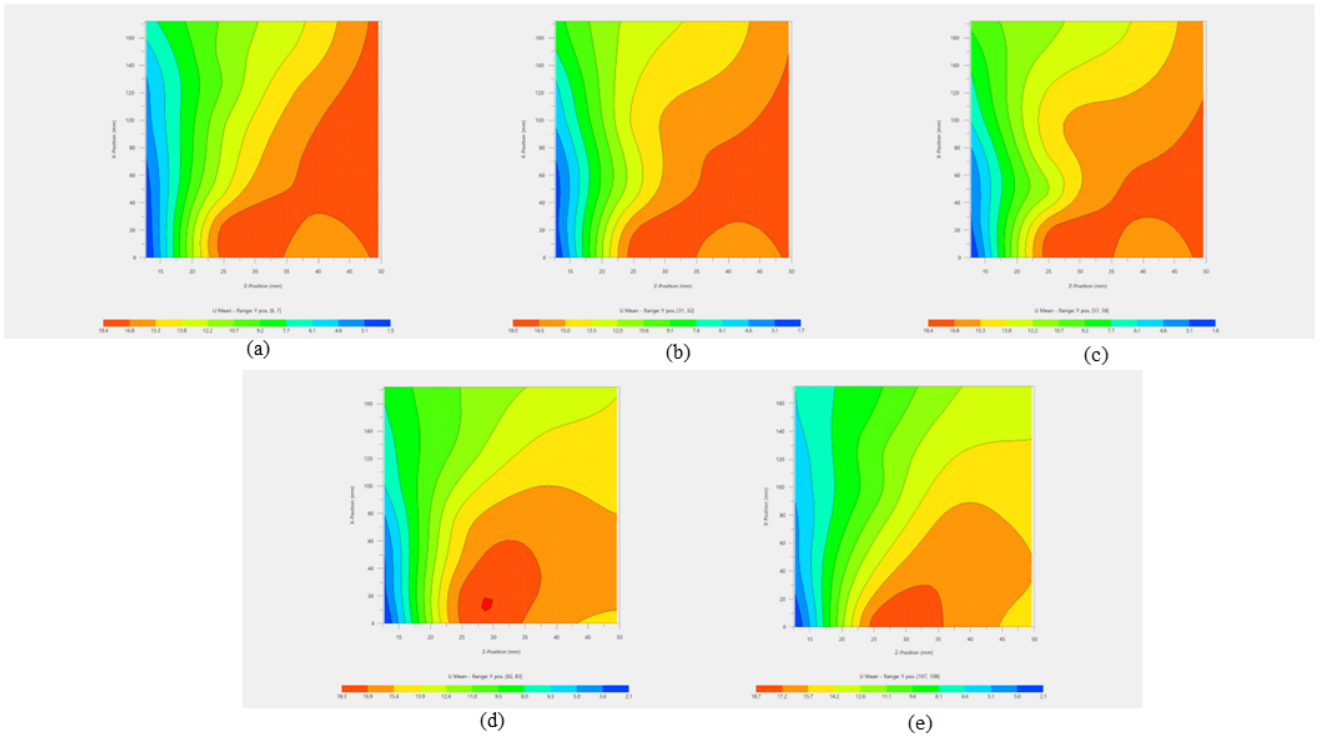

Fig. 13 Mean airflow velocity around the cylinder and cantilever plate at planes (a) Y = -6.34 mm, (b) Y = -31.75 mm, (c) Y = -57.15 mm, (d) Y = -82.55 mm, and (e) Y = -107.90 mm captured using CTA measurements at a wind tunnel free-stream velocity of 10 m/s.

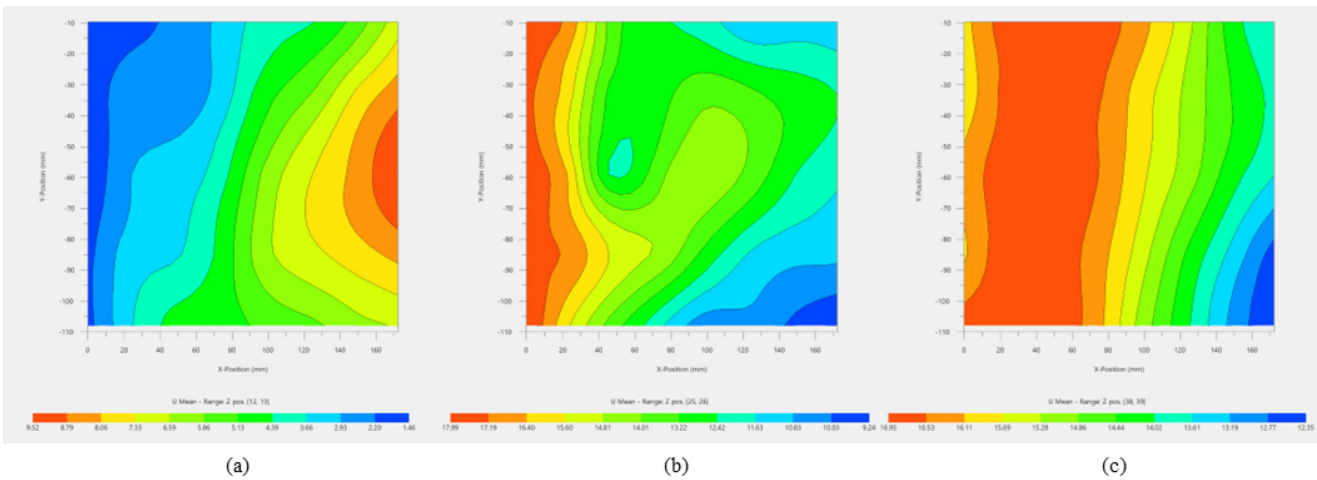

Fig. 14 Mean airflow velocity around the cylinder and cantilever plate at planes (a) Z = 12.69 mm, (b) Z = 25.39 mm, and (c) Z = 38.09 mm captured using CTA measurements at a wind tunnel free-stream velocity of 10 m/s.

the roving accelerometer was roved through each of the 37 nodes shown in Fig. 5. At each node, 30 s of accelerometer data and 35 s of CTA data were captured. The reference accelerometers were in the same positions as those of the EMA test as indicated by the red circles in Fig. 5. Siemens Testlab Version 2306 was used to perform the OMA, including data acquisition and curve fitting using the PolyMAX algorithm. The OMA experimental setup and equipment is shown in Figs. 15 and 16.

After completion of the OMA experiment, a CTA plot of the voltage versus time signal was plotted for the run in which the roving accelerometer was placed on the left-most node of the lower mounting bracket, as depicted in Fig. 5. Then, the

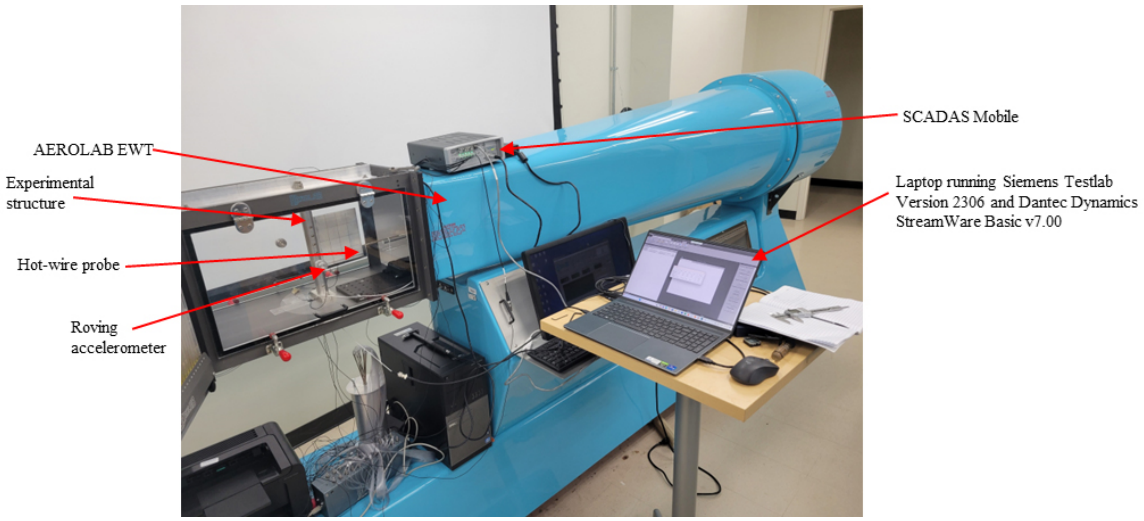

Fig. 15 OMA experimental setup and equipment including the AEROLAB EWT, experimental structure, hot-wire probe, roving accelerometer, SCADAS Mobile, and laptop running Siemens Testlab Version 2306 and Dantec Dynamics StreamWare Basic v7.00.

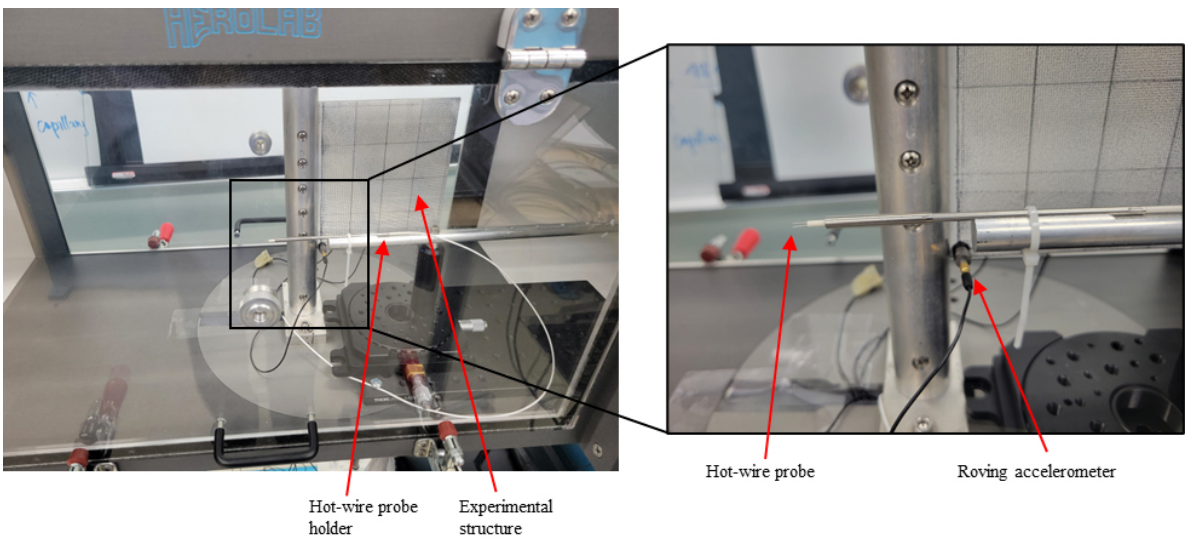

Fig. 16 OMA experimental setup inside the EWT test section showing the experimental structure, hot-wire probe, hot-wire probe holder, and roving accelerometer. The hot-wire probe is pictured in a position forward of the cylinder and cantilever plate for setting the wind tunnel free-stream velocity to 10 m/s.

power spectrum of the voltage versus time signal was calculated and plotted, where the power spectrum was calculated after applying a Hamming window and using 4096 bins with 75% overlap, yielding an uncertainty of 5.44%. The voltage versus time signal and the power spectrum are shown in Figs. 17 and 18, respectively. The peaks in Fig. 18 are specified by red circles, indicating the frequency content of the airflow at the hot-wire probe location. From the results shown in Fig. 18, the vortex shedding frequencies observed are 2.4 Hz, 18.3 Hz, and 40.3 Hz.

Testlab's PolyMAX algorithm was used to curve fit the cross-power functions that were derived from the accelerometer data captured during the OMA experiment using a curve fitting model size of 32 modes. The first two stable operational modes and their corresponding operational mode shapes were selected within a frequency band of 0-400 Hz, as shown in Figs. 19 and 20, respectively. As indicated in Fig. 20, mode 1 is the first bending mode of the cantilever plate and mode 2 is the first torsional mode of the cantilever plate.

Fig. 17 CTA plot of the voltage versus time signal.

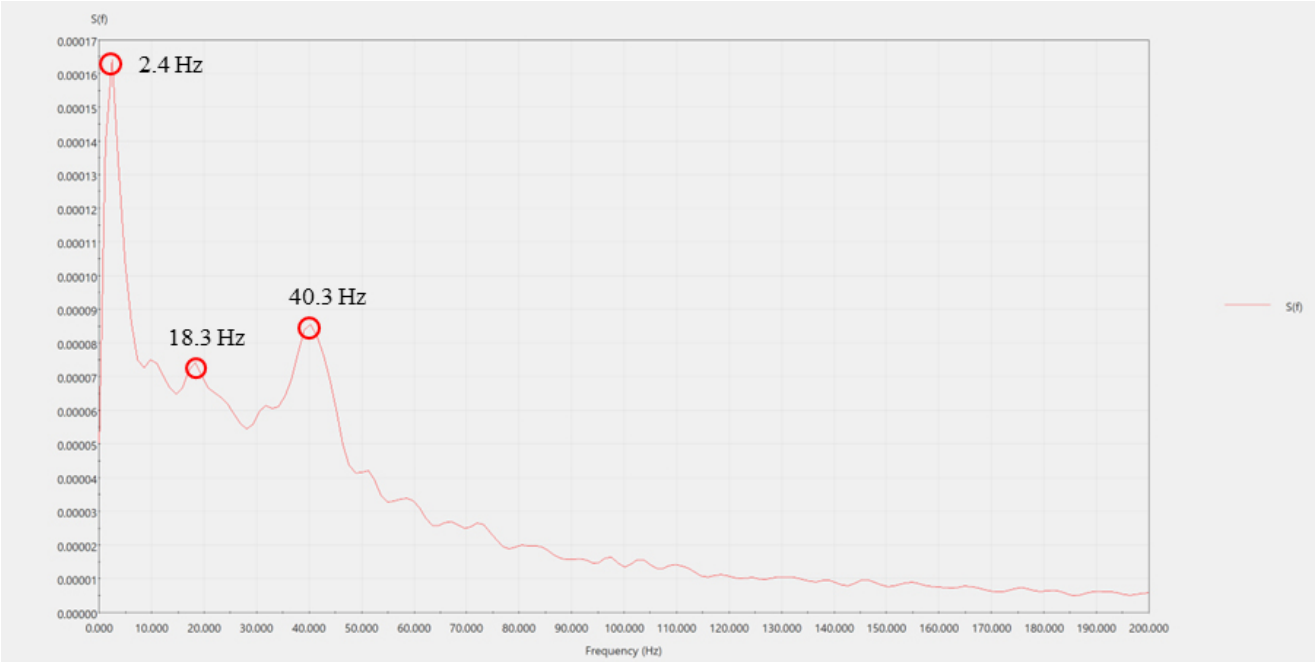

Fig. 18 CTA plot of the power spectrum of the voltage versus time signal shown in Fig. 17. The power spectrum was calculated after applying a Hamming window and using 4096 bins with 75% overlap. The frequencies at the circled peaks indicate the frequency content of the airflow.

Analysis

In this research, an experimental structure consisting of a cantilever plate fixed to a cylinder with an upper and lower mounting bracket was mounted in an AEROLAB EWT and characterized by performing a roving hammer EMA. The first three stable mode shapes were identified within a frequency band of 0-400 Hz, as shown in Fig. 7, which are consistent with

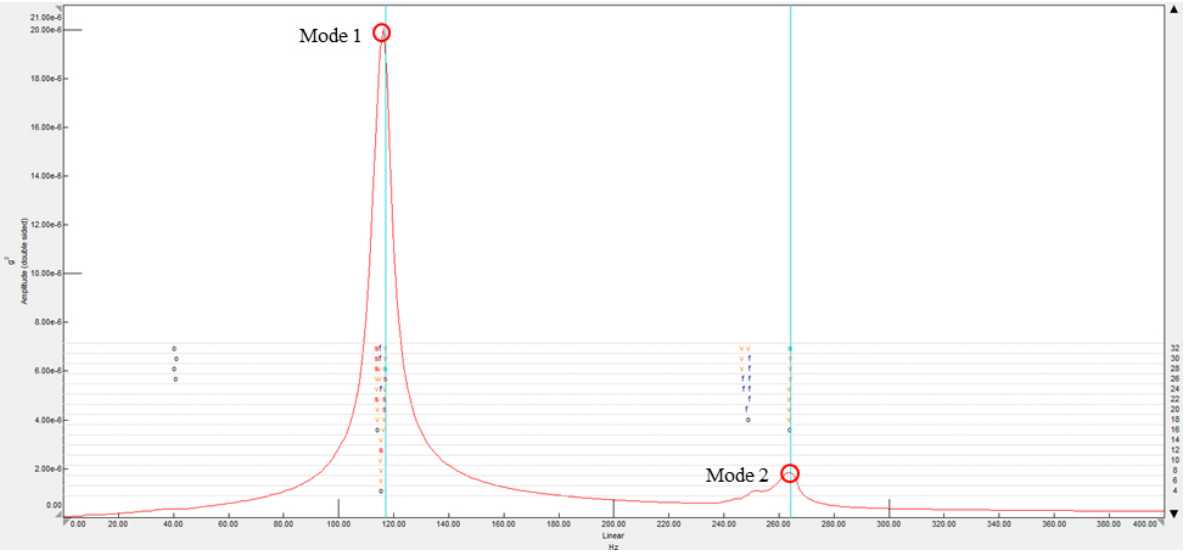

Fig. 19 Stabilization diagram using a curve fitting model size of 32 modes, where the first two stable operational modes between a frequency band of 0-400 Hz are indicated by red circles. The wind tunnel free-stream velocity was 10 m/s.

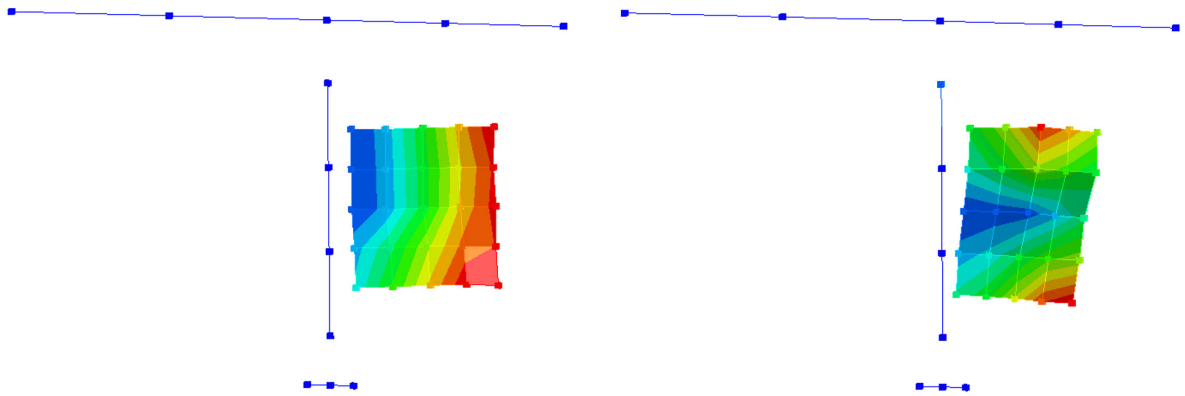

Fig. 20 First two stable operational mode shapes and their corresponding frequency and damping values within a frequency band of 0-400 Hz for a wind tunnel free-stream velocity of 10 m/s.

previous results [12]. Then, a CTA experiment was performed at a free-stream velocity of 10 m/s, allowing for visualization of the mean airflow velocity around the cylinder and cantilever plate. Fig. 12 shows that the mean airflow velocity is lower near the plate and increases to a maximum value exceeding that of the free-stream velocity at some distance away from the plate in the Z-direction, and then decreases back to the free-stream velocity. This phenomenon is due to a combination of boundary layer effects and vortex shedding, where in the former case the fluid velocity near a surface is lower than the velocity further away from the surface, and in the latter case the local airflow velocity is increased within a vortex. Similar results are observed in Figs. 13 and 14. An OMA was performed using a roving accelerometer and four reference accelerometers while the hot-wire probe collected data at a fixed position of X = 127.00 mm, Y = -31.75 mm, and Z = 25.39 mm. From the power spectrum plot in Fig. 18, the peak with the highest frequency of 40.3 Hz indicates the highest vortex shedding frequency observed at the probe location. Using Equation 1 or Fig. 2, the theoretical vortex shedding frequency expected for a 31.8 mm diameter cylinder in an airflow with a velocity of 10 m/s is 62.3 Hz. This case of reduced vortex shedding frequency observed in the experiment may be due to energy dispersion across several frequencies, as shown in Fig. 18 where there are peaks at 2.4 Hz, 18.3 Hz, and 40.3 Hz. From the results of the OMA shown in Fig. 20, the natural frequencies of the first two stable operational modes match very well with the first two stable modes captured from the EMA shown in Fig. 7. The percent difference between the mode 1 frequencies captured using EMA and OMA is 0.39% and the

percent difference between the mode 2 frequencies captured using EMA and OMA is 0.29%. These results are expected because the structure will vibrate at the same natural frequencies regardless of the excitation source. Finally, the third mode that was observed in Fig. 6 using the EMA method was not observed using the OMA method, as shown in Fig. 19, because the free-stream velocity of 10 m/s was not high enough to excite this third mode. Additional observable modes should be expected in the OMA results with higher free-stream velocities.

Conclusion

The aim of this FSI work was to explore the vibration response of a stiff cantilever plate attached to a cylinder in an AERO-LAB EWT under an airflow excitation. A roving hammer EMA was first used to characterize the structure by determining the first three out-of-plane natural frequencies and mode shapes within a frequency band of 0-400 Hz. Then, CTA was used to capture the mean airflow velocity around the cylinder and cantilever plate with a free-stream velocity in the wind tunnel of 10 m/s. Some interesting phenomena were observed in the mean airflow velocity plots that are attributed to boundary layer and vortex shedding effects. Lastly, the structure's response to a free-stream velocity of 10 m/s was captured by performing an OMA, where the first two natural frequencies had less than a 0.4% difference when compared to the first two natural frequencies captured using the EMA method.

Acknowledgments The authors would like to thank Dr. Zheng Li and Morgan State University for their support in allowing access to the AEROLAB EWT.

References

1. Modarres-Sadeghi Y (2022) Introduction to Fluid-Structure Interactions. Springer Nature, Cham.
2. Xie R, Yu L, Zhu W, Pan B (2020) Experimental study on flow-induced full-field vibration of a flexible splitter plate behind a cylinder using stereo-digital image correlation. J Vib Acoust. https://doi.org/10.1115/1.4048390
3. Wu J, Shu C, Zhao N (2014) Numerical study of flow control via the interaction between a circular cylinder and a flexible plate. J Fluids Struct. https://doi.org/10.1016/j.jfluidstructs.2014.06.002
4. Duan F, Wang J (2021) Fluid–structure–sound interaction in noise reduction of a circular cylinder with flexible splitter plate. J Fluid Mech. https://doi.org/10.1017/jfm.2021.403
5. Chutkey K, Suriyanarayanan P, Venkatakrishnan L (2018) Near wake field of circular cylinder with a forward splitter plate. J Wind Eng Ind Aerod. https://doi.org/10.1016/j.jweia.2017.11.019
6. Shukla S, Govardhan RN, Arakeri JH (2013) Dynamics of a flexible splitter plate in the wake of a circular cylinder. J Fluids Struct. https://doi.org/10.1016/j.jfluidstructs.2013.03.002
7. Ro KD (2014) Experimental characterization of the flow field of square prism with a detached splitter plate at high Reynolds number. J Mech Sci Technol. https://doi.org/10.1007/s12206-014-0621-5
8. Watine Y, Gabillet C, Lossouarn B, Deü JF, Astolfi JA (2023) Vortex-induced vibrations of a cantilevered blunt plate: POD of TR-PIV measurements and structural modal analysis. J Fluids Struct. https://doi.org/10.1016/j.jfluidstructs.2022.103832
9. Fernandez F, Cleaver D, Gursul I (2022) Unsteady aerodynamics of flexible wings in transverse gusts. J Fluids Struct. https://doi.org/10.1016/j.jfluidstructs.2021.103425
10. Ahn YJ, Eitner MA, Rafati S, Musta MN, Sirohi J, Clemens NT (2022) Experimental investigation of fluid-structure interaction in Mach 2 flow using simultaneous high-speed PIV and DIC. 20th Int Symp Appl Laser Imaging Tech Fluid Mech. https://par.nsf.gov/biblio/10357649
11. Abdi R, Rezazadeh N, Abdi M (2019) Investigation of passive oscillations of flexible splitter plates attached to a circular cylinder. J Fluids Struct. https://doi.org/10.1016/j.jfluidstructs.2018.11.001
12. Will DT, Zhu WD (2023) Experimental modal analysis and operational deflection shape analysis of a cantilever plate in a wind tunnel with finite element model verification. Exp Tech. https://doi.org/10.1007/s40799-023-00682-w
13. Massey BS, Ward-Smith J (1998) Mechanics of Fluids, 7th edn. Stanley Thornes (Publishers) Ltd, Cheltenham.
14. Munson BR, Young DF, Okiishi TH, Huebsch WW (2009) Fundamentals of Fluid Mechanics, 6th edn. John Wiley & Sons, Inc, Hoboken.